Geophys. J. Int. (2000) **141,** 401–412

Modelling teleseismic waves in dipping anisotropic structures

A. W. Frederiksen and M. G. Bostock

Department of Earth and Ocean Sciences, University of British Columbia, Vancouver, BC, V6T 1Z4, *Canada. E-mail: andyf@eos.ubc.ca*

Accepted 1999 December 1. Received 1999 November 27; in original form 1999 July 13

SUMMARY

The existence of seismic discontinuities within the continental upper mantle has long been recognized, with more recent studies often indicating an association with elastic anisotropy. Their near-vertical sampling renders teleseismic *P* and *S* waves suitable for characterization of mantle discontinuities, but computationally efficient methods of calculating synthetic seismograms are required for structures that exhibit lateral variability. We consider lithospheric models consisting of planar, homogeneous anisotropic layers with arbitrary dip. We adopt the traveltime equation of Diebold for dipping, plane-layered media as the basis for a high-frequency asymptotic method that does not require ray tracing. Traveltimes of plane waves in anisotropic media are calculated from simple analytic formulae involving the depths of layers beneath a station and the vertical components of phase slowness within the layers. We compute amplitudes using the reflection and transmission matrices for planar interfaces separating homogeneous anisotropic media. Modelling indicates that upper-mantle seismic responses depend in a complex fashion on both layer dip and anisotropy, particularly in the case of converted phases. Azimuthal anisotropy generally displays a distinctive 180° back-azimuthal periodicity in *Ps* conversion amplitude, as opposed to the 360° symmetry produced by dip. In contrast, anisotropy with a steeply plunging axis may under certain conditions be difficult to distinguish from interface dip, as both exhibit a 360° symmetry. We demonstrate the application of the method on *Ps* and *Sp* conversion data from the Yellowknife Array, which show evidence for both dipping and anisotropic layering, attributed to layers of anisotropic fabric in the upper mantle associated with ancient subducted slabs.

Key words: ray theory, seismic anisotropy, seismic wave propagation, Slave craton, upper mantle.

1 INTRODUCTION

Abrupt mantle velocity transitions between the Moho and the 410 km discontinuity have long been known to exist (Lehmann 1961; Hales 1969). Bostock (1999) gives a review of these features as observed beneath the continental lithosphere. The principal continental discontinuities to be widely observed are the Hales discontinuity, at a depth of ~60 km, which has commonly been ascribed to the spinel–garnet phase transition (Hales 1969; Revenaugh & Jordan 1991), and the Lehmann discontinuity (ranging from 210 to 300 km depth), which has been attributed to a transition between the anisotropic lithosphere and the more isotropic asthenosphere (Leven *et al.* 1981; Revenaugh & Jordan 1991; Karato 1992; Gaherty & Jordan 1995). Recently, a correspondence between these shallow mantle discontinuities and ancient, underplated former oceanic lithosphere in the continental root has been suggested on the basis of correlations with surface geology, significant dip on some interfaces (Bostock 1998) and anisotropic (~10 km thick) layering, interpreted to be stranded oceanic crust.

More accurate characterization of these upper-mantle structures requires a seismic modelling tool capable of handling both anisotropy and dipping structures, while being sufficiently economical to be usable in non-linear waveform inversions. Anisotropic reflectivity approaches (Booth & Crampin 1983; Fryer & Frazer 1984; Levin & Park 1997; Thomson 1997) are restricted to flat-lying structures and are computationally expensive. Conventional 3-D ray tracing (e.g. Červený 1972) relies on a high-frequency approximation of the wavefield and can handle non-horizontal interfaces. However, it generally requires shooting or bending techniques to isolate the correct ray and user input to avoid complications due to triplications. In this paper, we develop a computationally inexpensive, high-frequency method for modelling teleseismic wave propagation in homogeneous, plane-layered, dipping structures that is not dependent on shooting.

2 METHODOLOGY

The traveltime equation of Diebold (1987) is an analytic expression for the traveltime along an individual ray between source and receiver through a medium comprising isotropic plane-dipping layers in three dimensions. As suggested by Richards *et al.* (1991), this equation can provide the basis for an efficient ray-theoretical seismic modelling technique. Diebold's formula, derived for isotropic media, is written in the notation of Richards *et al.* (1991) as

$$T = -\mathbf{p}_A \cdot \mathbf{X}_A + \mathbf{p}_B \cdot \mathbf{X}_B + \sum_j (\xi_{aj} + \xi_{bj}) z_j \,, \tag{1}$$

where $\mathbf{p}_A$ and $\mathbf{p}_B$ are the horizontal slownesses of the ray at the source and receiver, respectively, $\mathbf{X}_A$ and $\mathbf{X}_B$ are distance vectors from an arbitrary vertical reference line to the source and receiver, z_j is the thickness of layer j at the vertical reference line, and ξ_{aj} and ξ_{bj} are the downgoing and upgoing vertical slownesses in layer j. The vectors $\mathbf{X}_A$ and $\mathbf{X}_B$ are parallel to the interfaces on which the source and receiver, respectively, are located [taking them to be horizontal vectors, as described in Richards *et al.* (1991), is erroneous; see Aldridge (1992)]. We begin by re-deriving a related equation for the teleseismic (i.e. plane wave) case using simple vector notation and demonstrate that, as suggested by Hake (1986), it is applicable to anisotropic media.

We consider a teleseismic (plane) wave front incident from below upon a medium consisting of dipping, planar and possibly anisotropic layers (Fig. 1). According to ray theory, the traveltime t along a ray Γ from the base of a general model to a receiver at the surface may be written as

$$t = \int_\Gamma \mathbf{p} \cdot d\mathbf{l} \,, \tag{2}$$

where $\mathbf{p}$ represents the phase slowness vector, which is perpendicular to the wave front (and, in the anisotropic case, not necessarily parallel to the ray). In a medium consisting of homogeneous layers, the path reduces to a series of straight-line segments, and the traveltime may be expressed as

$$t = \sum_{i=1}^{N} t_i - \tau = \sum_{i=1}^{N} \mathbf{p}_i \cdot \mathbf{l}_i - \tau \,, \tag{3}$$

where $\mathbf{p}_i$ is the phase slowness vector for the ith ray segment, $\mathbf{l}_i$ is the ray segment represented as a vector and τ is a time shift to a common reference time, chosen to be the time when the plane wave sweeps across the base of the layer stack immediately below the station (point B in Fig. 1). Note that this notation differs from that of Diebold (1987).

Introducing the assumption that the layer boundaries are planar, the ray length vector $\mathbf{l}_i$ in any layer may be decomposed into vertical and interface-parallel portions $\mathbf{z}_i$ and $\mathbf{s}_i$ (Fig. 2). By Snell's law, the component of phase slowness parallel to an interface is preserved across the interface; hence, the traveltime in a single layer may be written

$$\begin{aligned} t_i &= \mathbf{p}_i \cdot \mathbf{l}_i = -\mathbf{s}_i \cdot \mathbf{p}_i - \mathbf{z}_i \cdot \mathbf{p}_i + \mathbf{s}_{i+1} \cdot \mathbf{p}_i \\ &= -\mathbf{s}_i \cdot \mathbf{p}_i - \mathbf{z}_i \cdot \mathbf{p}_i + \mathbf{s}_{i+1} \cdot \mathbf{p}_{i+1} . \end{aligned} \tag{4}$$

The time correction τ may be decomposed in a similar fashion into interface-parallel and wave front-parallel components, with the latter making no contribution to the traveltime; hence,

$$\tau = \mathbf{p}_b \cdot \mathbf{l}_b = -\mathbf{s}_1 \cdot \mathbf{p}_b + \mathbf{w}_b \cdot \mathbf{p}_b = -\mathbf{s}_1 \cdot \mathbf{p}_b = -\mathbf{s}_1 \cdot \mathbf{p}_1 \,. \tag{5}$$

Inserting expressions (4) and (5) into (3) yields

$$t = \sum_{i=1}^{N} (-\mathbf{s}_i \cdot \mathbf{p}_i - \mathbf{z}_i \cdot \mathbf{p}_i + \mathbf{s}_{i+1} \cdot \mathbf{p}_{i+1}) + \mathbf{s}_1 \cdot \mathbf{p}_1 \,, \tag{6}$$

which, as $\mathbf{s}_{N+1} = \mathbf{0}$, simplifies to

$$t = -\sum_{i=1}^{N} \mathbf{p}_i \cdot \mathbf{z}_i = \sum_{i=1}^{N} \xi_i z_i \,, \tag{7}$$

where ξ_i is the absolute value of the vertical slowness component for segment i and z_i is the thickness of the layer corresponding to segment i.

The calculation of vertical slownesses ξ_i required for the traveltime equation may be performed concurrently with the determination of the ray amplitudes through eigenvector decomposition of the system matrix (Kennett 1983; Fryer & Frazer 1984). For each interface, the system matrices $\mathbf{A}_i$ and $\mathbf{A}_{i+1}$ below and above the interface in an interface-parallel coordinate system may be expressed in terms of the elastic tensor c_{ijkl} for each layer, the layer densities, and the interface-parallel

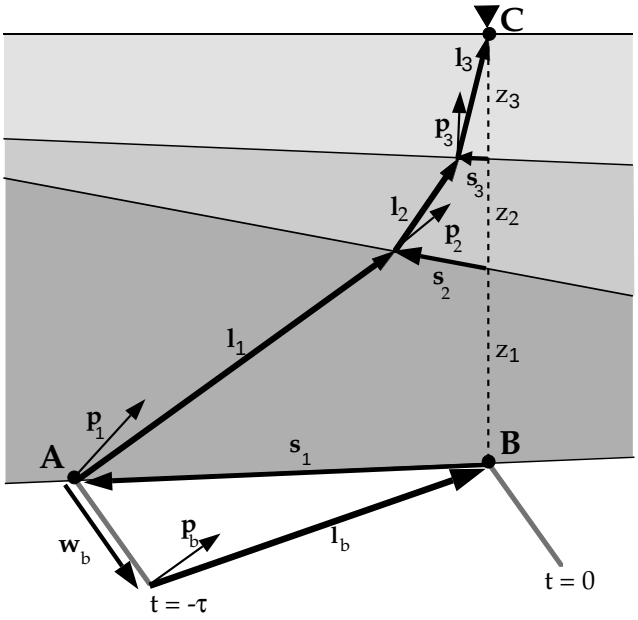

Figure 1. Ray-path decomposition for a transmitted phase in a three-layer model, simplified to two dimensions.

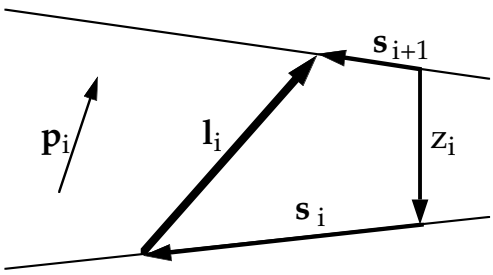

Figure 2. A single ray segment, decomposed into vertical and interface-parallel components.

slowness components (Woodhouse 1974; Fryer & Frazer 1984). The eigenvalues of these system matrices are the interface-perpendicular components of slowness for each phase, and the eigenvectors may be combined to form a scattering matrix used to calculate the reflection and transmission coefficients.

The procedure for determining the traveltime and amplitude of a given phase (transmission, conversion or multiple) is as follows: vertical slowness components and reflection/transmission coefficients for each segment and interface are determined through a sequence of eigenvector decompositions and coordinate-system rotations, proceeding segment by segment. The amplitude of a given phase is simply the product of appropriate reflection/transmission coefficients, while the traveltime is determined from eq. (7) using the calculated vertical slownesses. Combining all phases of interest, a displacement seismogram $\mathbf{u}(t)$ comprising M phases, each consisting of N_i segments, may be written as

$$\mathbf{u}(t) = \sum_{i=1}^{M} \mathbf{F}_i \mathbf{w}_i \left(\prod_{j=1}^{N_i} S_j^i \right) \delta \left(t - \sum_{k=1}^{N_i} \xi_k^i z_k^i \right), \tag{8}$$

where S_j^i is the appropriate reflection/transmission coefficient for phase i and the interface preceding segment j, $\mathbf{F}_i$ is the free-surface transfer matrix appropriate to phase i (which depends on the slowness vector in the uppermost layer; see e.g. Kennett 1991) and $\mathbf{w}_i$ is an upgoing 3×1 wave vector with one non-zero element corresponding to the wave type of the final segment of phase i. No shooting is required, and the resulting traveltimes and amplitudes are exact within the usual assumptions inherent in ray theory. Note that the formulation applies to both directly transmitted waves and phases involving multiple reflection.

The limitations of this method result from its underlying assumptions. In addition to the obvious restrictions of ray theory and homogeneous layers, the assumption that the incident wave may be approximated as planar restricts its utility to teleseismic waves in the upper mantle and crust, where the curvature of the wave front is minimal. Furthermore, the planar, dipping-layer assumption is reasonable for single stations where lateral sampling is limited, but it may be inadequate when considering array data in the presence of more general (e.g. folded) layering. Moreover, a steep interface ($\sim 50^\circ$ or more) at depth can present problems, as updip arrivals may miss it entirely due to a pinch-out, while downdip arrivals may arrive above the interface, rather than below.

3 MODELLING RESULTS

Previous workers have investigated the effects of anisotropy and layer dip on teleseismic wave propagation separately, but not in combination (Langston 1977; Cassidy 1992; Levin & Park 1998; Savage 1998). Both factors lead to backazimuthal variations in impulse response, involving traveltime and amplitude, as well as the rotation of *P–SV* energy onto the transverse component. Hexagonal anisotropy with a horizontal symmetry axis (i.e. azimuthal anisotropy) typically produces four-lobed backazimuthal patterns with 180° symmetry. However, this symmetry breaks as dip increases, producing a dominantly two-lobed (360°) pattern for 45° inclination (Levin & Park 1998). An isotropic dipping layer will produce a similar 360° periodicity in azimuth, and also causes rotation of energy from an initial *P* or *SV* arrival onto the transverse component. This latter effect is only reproducible in laterally homogeneous anisotropic layers when the uppermost layer is anisotropic. Modelling of the teleseismic *S* response has been restricted largely to simplified predictions of shear-wave splitting parameters for horizontally layered cases (e.g. Silver & Savage 1994; Rümpker & Silver 1998).

To examine the interaction of anisotropy and layer dip, we consider two classes of models (Fig. 3): wedge models, consisting of an isotropic crust underlain by a wedge of anisotropic upper mantle, and slab models, in which a dipping anisotropic layer is embedded in isotropic ambient mantle and overlain by an isotropic crust. Fixed properties of the models are given in Table 1. As the number of independent variables in these models is large, we fix the thickness of the layers, assume hexagonal symmetry and a prolate phase velocity surface in the anisotropic layers, and vary only the interface dip and the trend and plunge of the fast anisotropic axis. The anisotropy is parametrized as a percentage variation in *P*- and *S*-wave velocity, in the manner described by Farra *et al.* (1991), while the remaining parameter η is fixed at a value of 1.03. As in all synthetics in this paper, the filtered impulse responses have been transformed into the *P–SV–SH* wave vector domain, as defined by the horizontal slowness of the incident wave in the underlying half-space, to separate different phases more clearly. This procedure would be equivalent to eliminating the premultiplication by $\mathbf{F}_i$ in eq. (8) if the model were horizontally layered. In the dipping-layer situation, the procedure involves replacing $\mathbf{F}_i$ with the transfer matrix appropriate for the half-space slowness. Patterns detected in the *P*, *SV*

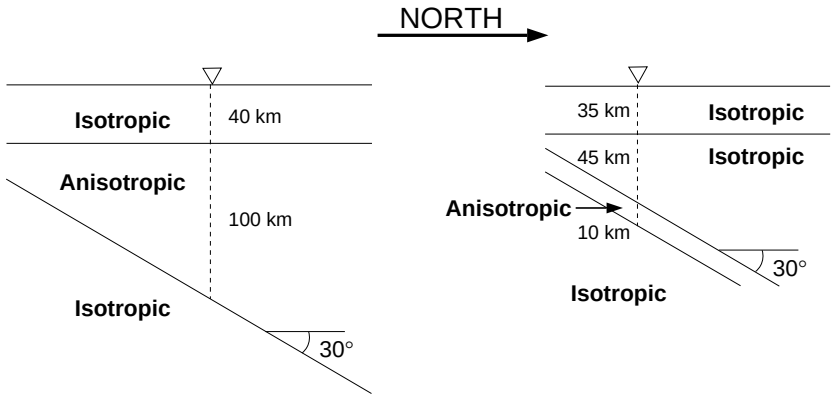

Figure 3. The simple wedge (left) and slab (right) structures used in forward modelling.

Table 1. Properties of synthetic models, as defined in Farra *et al.* (1991). α and β are in m s^{-1}, ρ in kg m^{-3} and z (thickness) in km. The percentage anisotropy is the same for P and S; the remaining parameter η is fixed at 1.03.

	Wedge model					Slab model				
Layer	z	α	β	ρ	Per cent anisotropy	z	α	β	ρ	Per cent anisotropy
1	40	6540	3710	2600	–	35	6540	3710	2600	–
2	100	8100	4500	3500	5.5	45	8100	4500	3500	–
3	–	8100	4500	3500	–	10	8100	4500	3500	5.5
4						–	8100	4500	3500	–

and *SH* components are similar to those visible in the vertical, radial and transverse components, respectively. However, presentation in this 'quasi'-wave vector domain provides a clearer separation of the principal phases than the displacement domain does, improves the visibility of low-amplitude phases (e.g. *Sp* conversions) and is also our preferred approach to the display and analysis of real data (see next section).

Fig. 4 shows the filtered impulse responses of variants of the wedge model to an incident teleseismic *P* plane wave, plotted as a function of backazimuth for a fixed incident horizontal slowness (0.05 s km^{-1}, equivalent to an incidence angle of 24°). From left to right, the three models plotted have anisotropic fast axes oriented west, north and north with a 30° plunge, while the base of the wedge dips 30°N. The *P* and *SV* components of these models are largely unaffected by the anisotropy, in part due to the presence of crustal multiples that mask the *Ps* conversion from the base of the anisotropic wedge at ~31 s reference time. The wedge-base conversion is only faintly visible on the *SV* component (mainly in the third panel). The *SH* component is more complex than *SV*. In particular, the direct *P* arrival appears in a two-lobed pattern, an effect produced by the dipping interface, as indicated by the fact that its polarity remains unchanged after a 90° rotation of the anisotropic symmetry axis. By contrast, the character of the Moho *Ps* conversion is anisotropy-controlled and the symmetry axis' orientation controls the polarity of its four-lobed pattern. The pattern loses its 180° symmetry in the dipping-axis case. The *Ps* conversion off the base of the wedge is the most complex, in that it displays a dip-controlled traveltime variation, a polarity pattern governed by the fast-axis location, and a doubled arrival indicating the splitting of the shear wave into qS_1 and qS_2 phases. The backazimuthal behaviour of the multiples appears to be dictated by the conversion interface (Moho or free surface); thus, Pp_mp (not converted) and Pps_ms (free-surface conversion) display two-lobed patterns, while P_ms, Pp_ms, and Ps_ms (Moho conversions) are four-lobed.

Fig. 5 shows *P* impulse responses for four variants of the slab model. The first three models contain a slab dipping 30° to the north, with the anisotropic symmetry axes oriented east, north, and north with a 30° plunge, respectively. The fourth model has a horizontal slab in which the fast axis plunges 30° to the north. As before, the main evidence of dip and anisotropy is on the *SH* component, due to the high amplitudes of crustal multiples on the *SV* and *P* components. The slab has parallel top and bottom interfaces with identical velocities above and below, and therefore transmitted phases that do not convert within the slab are not rotated onto the transverse component, because the upper interface cancels the effect of the lower interface. The principal features of note are therefore the *Ps* conversions produced by the top and bottom slab boundaries. These conversions form a pair of oppositely signed arrivals with identical backazimuthal dependence. The two horizontal-axis models differ only in polarity; pointing the axis downdip alters the effective anisotropy to near-vertical rays and so changes the amplitude pattern. A horizontally layered model with identical anisotropy displays a similar amplitude pattern, but is distinguishable through its lack of significant traveltime variation in backazimuth, a difference which may be difficult to detect in real data.

An interesting question that arises from this modelling is whether pathological cases exist where interface dip and anisotropy are practically indistinguishable to *Ps* conversions. Azimuthal or near-azimuthal anisotropy produces a diagnostic four-lobed *SH*-component pattern in backazimuth; however, an axis of symmetry that dips at ~45° produces a two-lobed pattern reminiscent of the effect of a dipping interface (Levin & Park 1997). Fig. 6 shows *Ps* conversions from two highly dissimilar models: a 5 per cent anisotropic, laterally homogeneous 10-km-thick lower crust whose axis of symmetry dips 55° to the north, sandwiched between isotropic crust and mantle (left panel), and a high-velocity, 10-km-thick lower-crustal wedge whose upper and lower interfaces dip 15° to the north and south, respectively (right panel.) The only apparent difference in polarity pattern between the resulting impulse-response panels is the rotation of the direct *P*, which occurs only in the presence of layer dip. Furthermore, the backazimuthal variation in *Ps* traveltime differs in phase by 180° between the two models. These distinctions might be difficult to isolate in real data.

Modelling teleseismic *S* impulse responses requires knowledge of the polarization of the incident wave. With this in mind, we have calculated impulse responses for incident *SV*- and *SH*-polarized waves. Fig. 7 shows the incident-*SV* and incident-*SH* responses for the wedge model, with a basal dip of 30° to the north and the anisotropic fast axis pointing downdip. Notable features are the splitting of the *S* wave into two arrivals, and the *Sp* conversion off the wedge base. The direct *S* shows the qS_1–qS_2 split in the anisotropic layer in the form of two separate arrivals with a significant traveltime difference, forming a four-lobed backazimuthal pattern with energy rotation into and out of the *P*–*SV* plane, and little evidence of a dip effect except in the faint rotation of the direct *S* phase onto the *P* component. *Sp* conversions originate at both the Moho and the base of the wedge. The former is faint and shows dip-controlled polarity, while the latter is also weak, displays considerable backazimuthal variation in traveltime, and shows a two-lobed amplitude pattern. The corresponding slab model displays similar features (Fig. 8; also with a downdip symmetry axis). Double arrivals (top and bottom of the slab) are visible on the *Sp* conversion, as well as a very small split in the transmitted *S*.

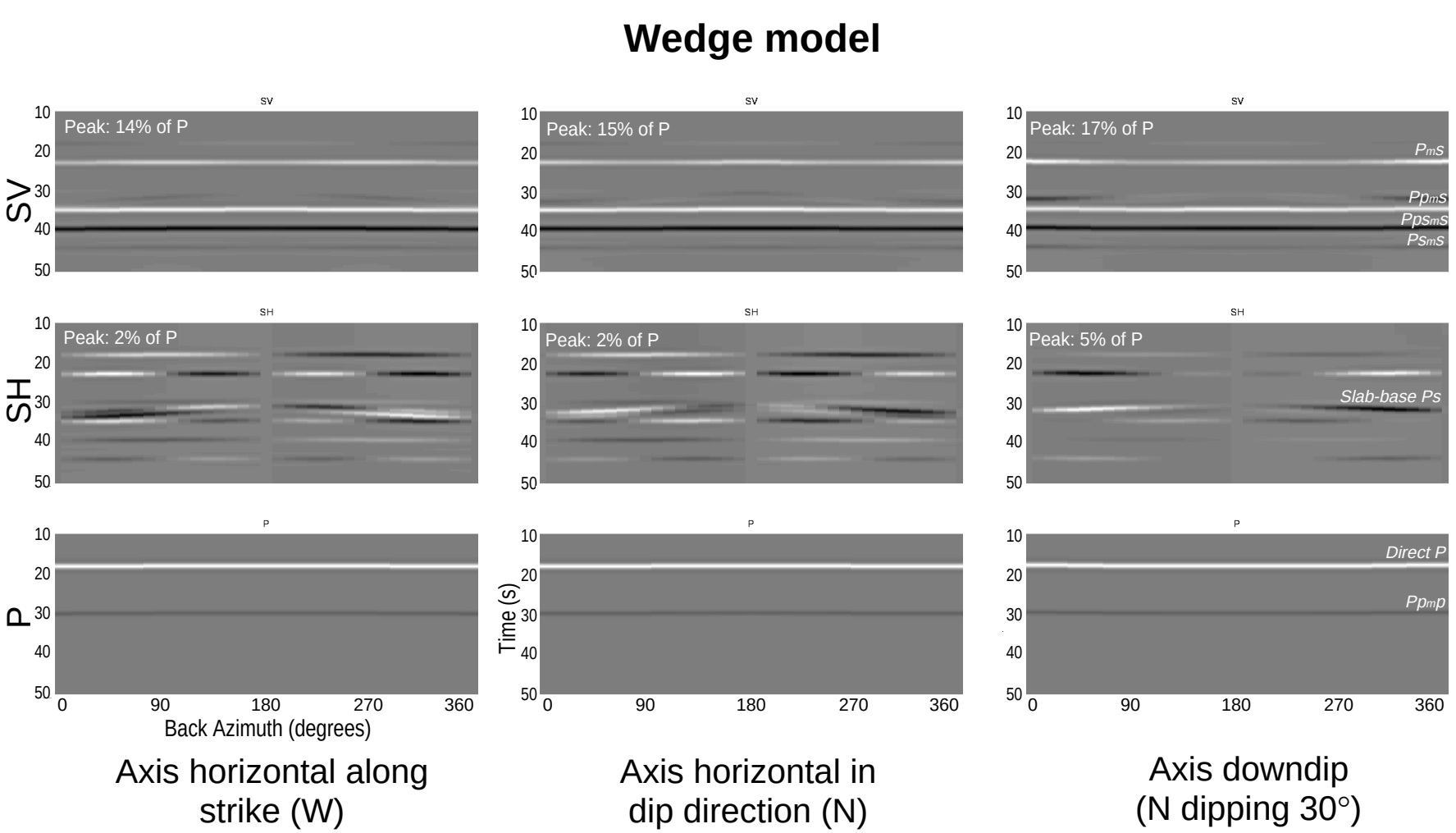

Figure 4. Impulse response to incident P wave at 0.05 s km^{-1} horizontal slowness (equivalent to an incidence angle of 24°) for three variants of the wedge model. Each trio of panels represents a backazimuth suite of three-component seismograms rotated into a P–SV–SH domain (see text for details); white regions are positive arrivals, black are negative arrivals. Timing of phases in this and subsequent figures is relative to the time when the incident plane wave crosses the deepest interface below the station; see Fig. 1.

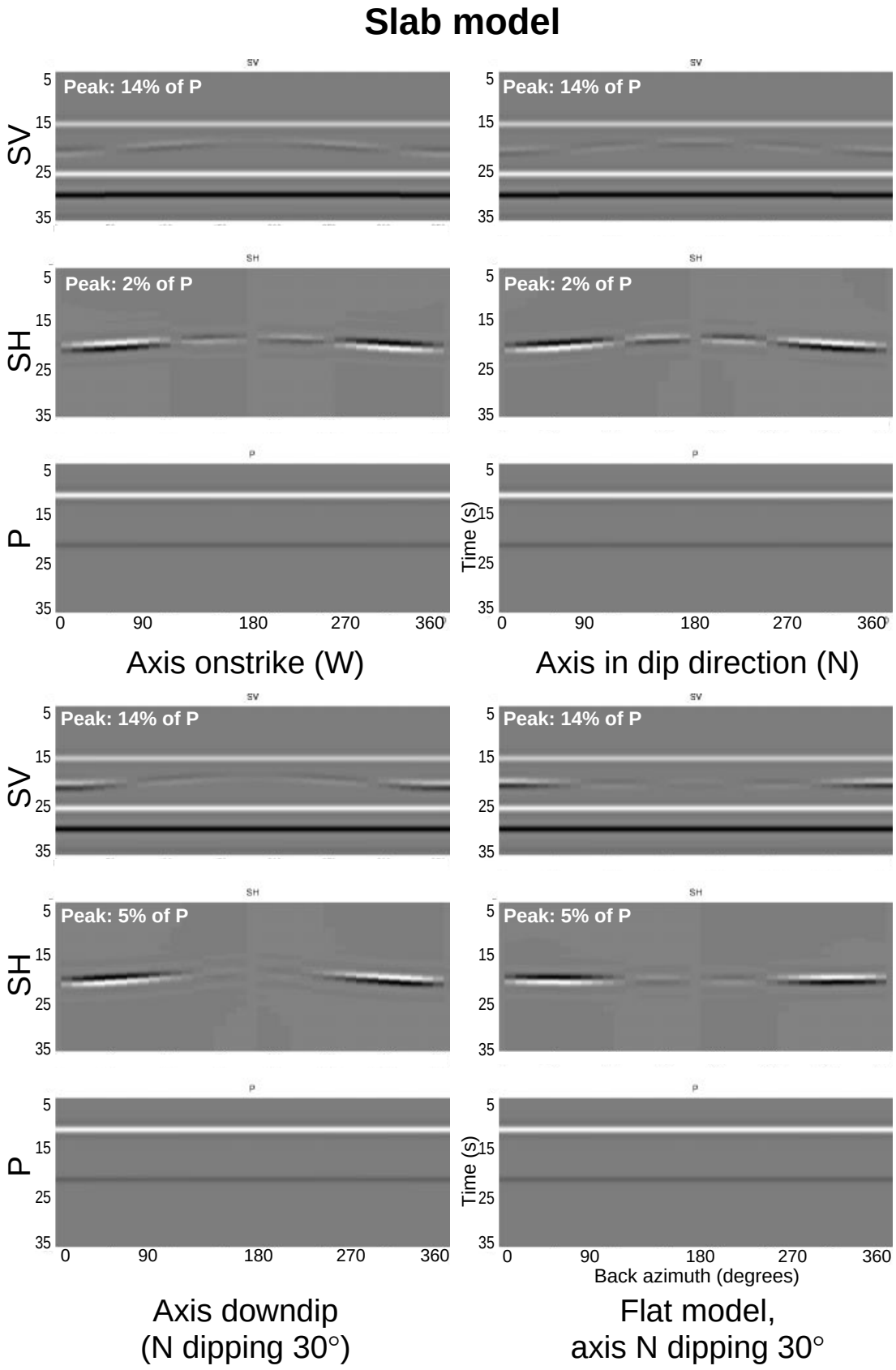

Figure 5. Impulse response to incident *P* wave at 0.05 s km^{-1} horizontal slowness (24° incidence) for three variants of the slab model.

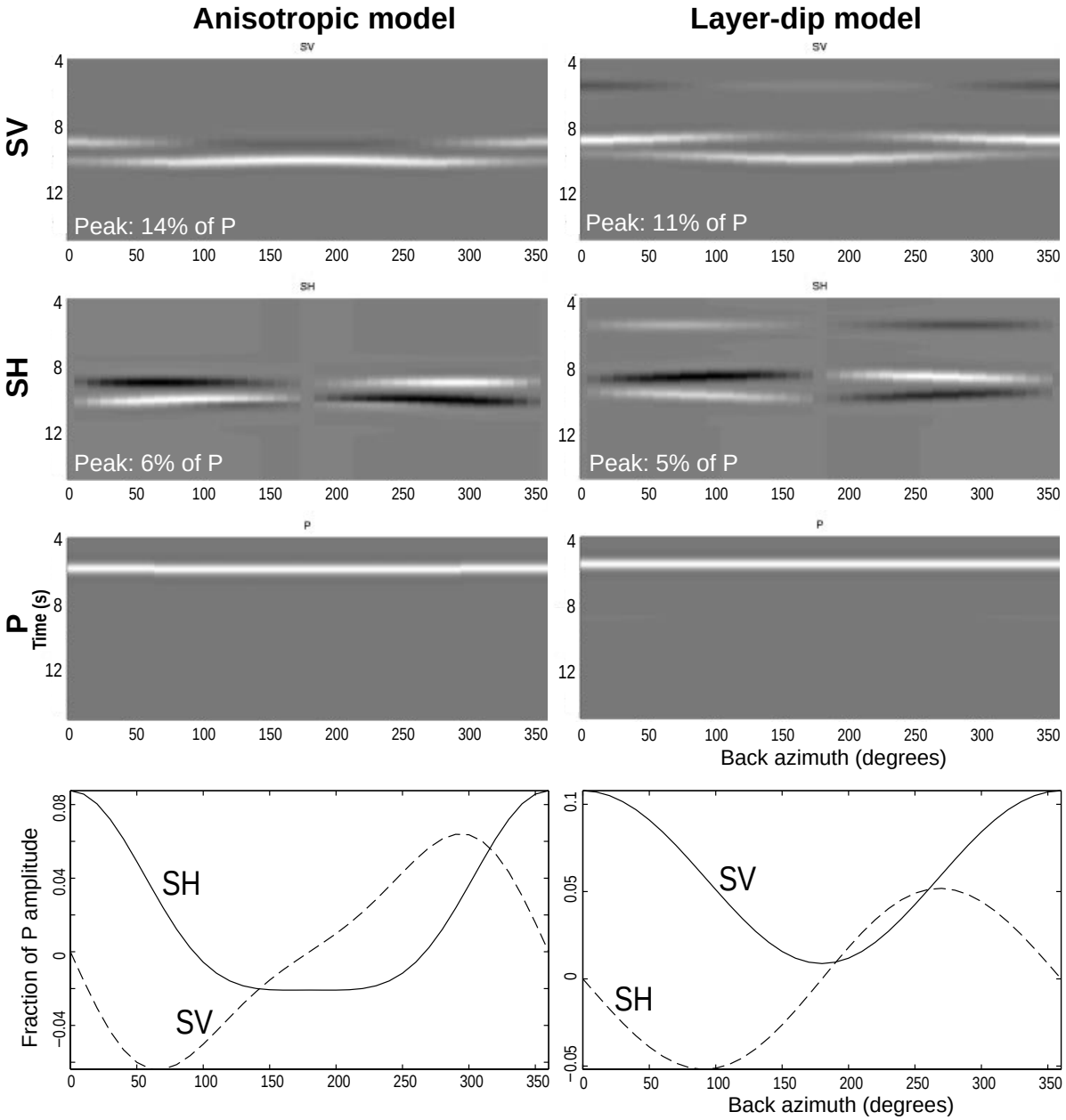

Figure 6. A demonstration of how, in the case of a near-vertical incident wave, the *P* impulse response of a flat anisotropic model can resemble that of a model with dipping layers. The line graphs at the bottom of the figure compare *SV* and *SH* amplitudes (relative to *P*) for the first-arriving conversion. The models are described in the text; the incident slowness used was 0.05 s km^{-1}.

These modelling results show that the interaction between layer dip and anisotropy can be complicated, even for simple models. For *Ps* conversions, crustal multiples are a problem in that they mask upper-mantle conversions. Most accessible information concerning anisotropy is contained in the amplitudes of the transverse component, while layer dip dominates backazimuth traveltime variations. Transverse-component polarity shifts are useful in locating the horizontal orientation of the anisotropic axis of symmetry, although its dip is more difficult to constrain. Note also that in more complicated situations, where two or more anisotropic layers are considered, the polarity crossovers do not, in general, exhibit such a simple relation to axis orientation. *S*-wave impulse responses contain information on anisotropy in the form of shear-wave splitting, and in addition, *Sp* conversions are strongly sensitive to layer dip. However, this sensitivity may prove difficult to observe due to their low amplitudes and the ubiquitous presence of signal-generated noise in the form of the *P* coda.

4 APPLICATION TO SLAVE CRATON DATA

The Yellowknife Array (YKA), Northwest Territories, Canada, has recorded three-component data at four broad-band stations since 1989. It is well situated with respect to global seismicity, in that it has recorded teleseismic events from a broad range of backazimuths (Fig. 9). Bostock (1998) analysed a comprehensive *Ps* data set from the YKA and found evidence of both anisotropic layering and dipping interfaces in the upper

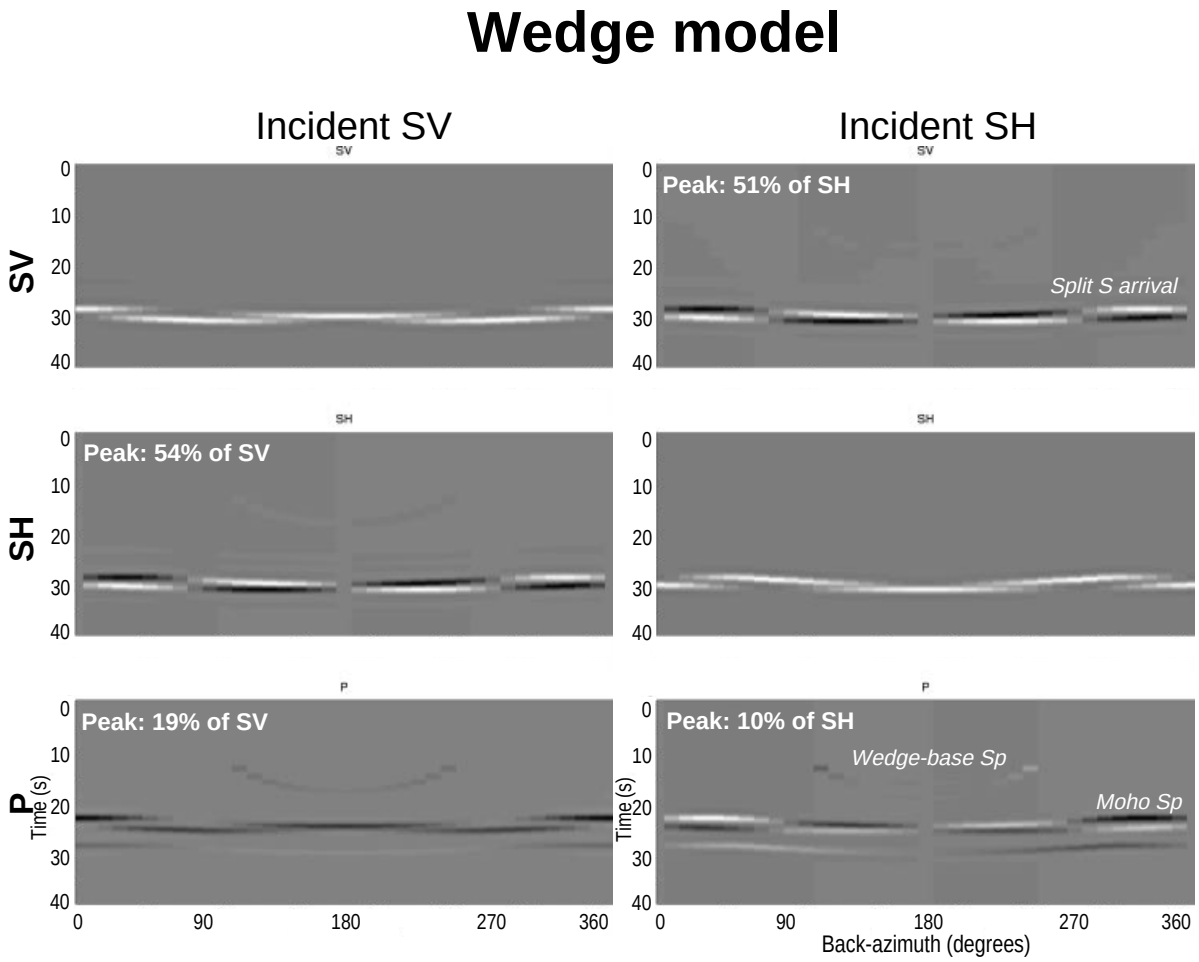

Figure 7. *SV* and *SH* impulse responses of the downdip-axis variant of the wedge model at an incident slowness of 0.09 s km^{-1} (equivalent to an incidence angle of 24°). Note the limited backazimuth window (100°–250°) in which the *Sp* arrival from the dipping interface appears. Outside this window, the phase is supercritical.

mantle. The YKA *P* and *S* data set thus provides a useful test for our modelling technique.

Fig. 9 displays the full set of *Ps* data for one of the YKA stations (YKW3), binned, transformed into the *P–SV–SH* domain, as described earlier, and source-normalized. Source normalization is performed through simultaneous deconvolution of all seismograms within a given bin, as described in Bostock (1998). We used approximately 361 seismograms to generate the *SV* and *SH* panels, each comprising 143 impulse responses. We display these responses sorted in an order determined by counting outwards from the station in successive backazimuthal swathes, with the geographic distribution of bins shown in Fig. 9(f). The *SV* and *SH* impulse response panels (Figs 9a and c) are compared to synthetics (Figs 9b and d) developed through trial and error with good qualitative agreement. Table 2 presents the model used.

Table 2. Properties of YKW3 model. All anisotropic layers have horizontal symmetry axes, and all interfaces are horizontal, with the exception of layer 9, whose upper and lower interfaces strike at −70° and dip 25°, and whose symmetry axis plunges 25°.

Layer	Thickness (km)	α (m s^{-1})	β (m s^{-1})	ρ (kg m^{-3})	Per cent anisotropy	Axis trend (°)
1	36	6200	3650	2600	–	–
2	44	8100	4500	3500	–	–
3 (H)	10	8100	4500	3500	5.5	100
4	41	8100	4500	3500	–	–
5 (X)	5	8100	4500	3500	5.5	165
6 (X)	10	8100	4500	3500	–	–
7 (X)	5	8100	4500	3500	5.5	75
8	49	8100	4500	3500	–	–
9 (L)	5	8150	4530	3500	5.5	20
10	–	8150	4530	3500	–	–

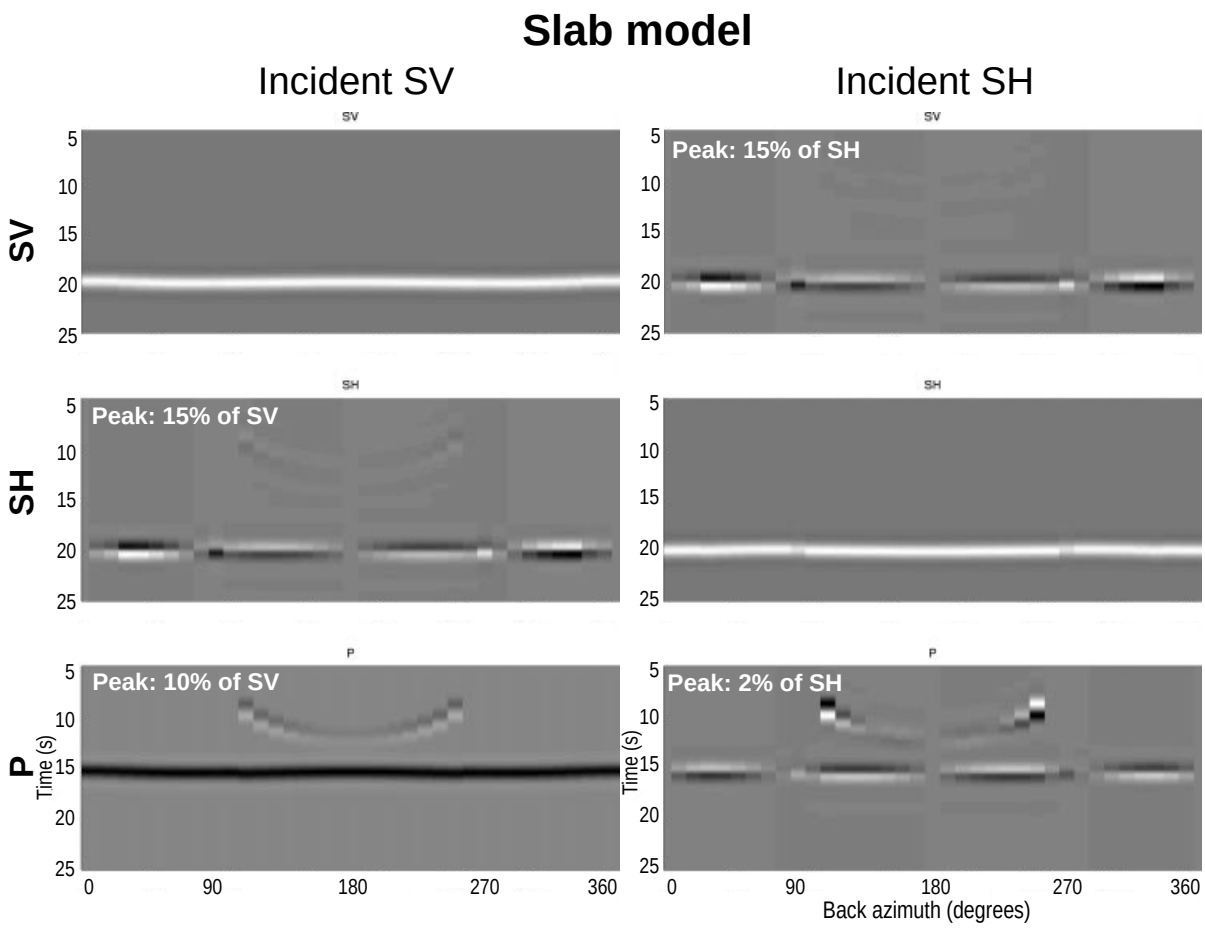

Figure 8. *SV* and *SH* impulse responses at an incident slowness of 0.09 s km^{-1} (24° incidence) for the downdip-axis variant of the slab model.

The principal features of the model are as follows: an isotropic 36-km-thick crust overlies a mantle in which layers of hexagonally symmetric anisotropic fabric are embedded. The first anisotropic layer (H) occurs at 80 km depth over a 10-km-thick interval with the horizontal axis pointing east. Crossovers in polarity near 310° backazimuth on the *SV* component and at 180° and 270° on the *SH* component constrain the orientation of this axis. A pair of 5-km-thick anisotropic layers separated by 10 km of isotropic material occur at 131 km depth, reproducing the feature marked as X. The anisotropy axis orientations of the upper and lower layers at 165° and 75°, respectively, are required to reproduce this complex arrival if the anisotropy is assumed to be prolate (i.e. the fast direction is assumed to be the symmetry axis). At 193 km depth a final anisotropic layer (L) dips at 25° to the northeast. The nature and dip of these layers are consistent with the interpretation that they represent the remains of ancient subducted oceanic crust. As this model differs little from the one in Bostock (1998), it will not be discussed further here.

Analysis of *Sp* data is somewhat more complicated due to (i) the source-dependent polarization of the incident *S* wave; (ii) higher levels of signal-generated noise (see e.g. Vinnik & Romanowicz 1991; Bock 1994) and (iii) low energy levels at frequencies above 0.2 Hz from all but very deep events. The data set is therefore greatly reduced in numbers relative to *P*. We have confined our attention to two of the best events available for YKA and have detailed these in Table 3. Source-dependent polarization precludes effective use of deconvolution procedures, because each *S* trace results from two impulse responses and two source functions (*SV* and *SH*). Instead, we transformed *S* seismograms into the *P*–*SV*–*SH* wave vector domain as defined by the horizontal slowness predicted from a 1-D earth model, and estimated the incident *SV* and *SH* waveforms by taking windows around the direct *S* arrival on the *SV* and *SH* components. We convolved these waveform estimates with *P* impulse responses derived from the model in Table 2 and summed the convolved traces to form a synthetic *P* component for comparison with the data. Fig. 10 shows

Table 3. Events used for *Sp* conversion analysis at station YKW3.

Region	Date	Time	Latitude	Longitude	Depth	Magnitude
Izu-Bonin Trench	96/06/26	03:22:03	27.73°N	139.75°E	469 km	5.5
Afghanistan	94/06/30	09:23:21	36.33°N	71.13°E	227 km	6.1

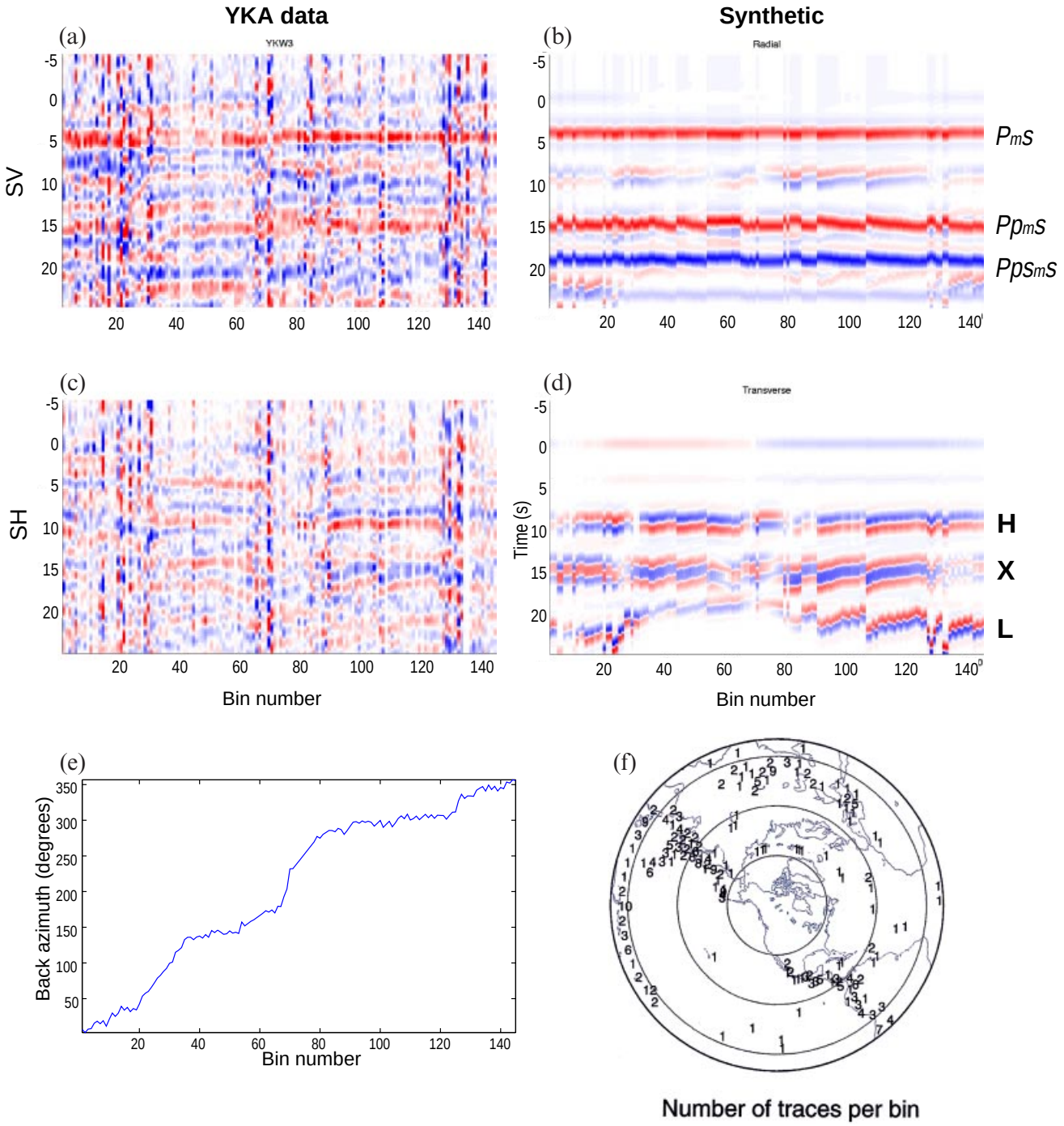

Figure 9. Deconvolved *P* data (a and c) from YKA station YKW3 (Bostock 1998) compared to the filtered synthetic impulse response (b and d) of the model described in Table 2. Data from events of similar backazimuth and epicentral distance are binned together; the bins are sorted by counting outwards from the stations in successive backazimuth swathes. The map in (f) shows the number of traces in each bin, while plot (e) relates the bin number to backazimuth. Principal phases are indicated on the synthetic. The *SV* component (a and b) is dominated by multiples Pp_ms and Pps_ms, while the *SH* component (c and d) is dominated by the anisotropic upper-mantle features H, X and L. The traveltime misfit of Pps_ms ($\sim$20 s) may be indicative of a more complex Moho than presented in the model.

this comparison. The Moho *Sp* conversion is strong, and there are indications that the mantle structure modelled for *P* contributes significantly to the response. In particular, the structure termed H appears to be responsible for the reasonable match on the Izu-Bonin event between -5 and -10 s, whereas deeper structure (X) near 131–141 km depth matches the signal near -15 s for the Afghanistan event. Note also that the H structure produces impulse responses for *SV* and *SH* in the Izu-Bonin event, which partially cancel when summed. A better fit to these data was achievable, but at the expense of the fit to the *Ps* data. It is clear from the *P*-component data in Fig. 10 that, even for these high-quality *S* events, high levels of signal-generated noise pose a significant limitation to the retrieval of mantle structure using *S*.

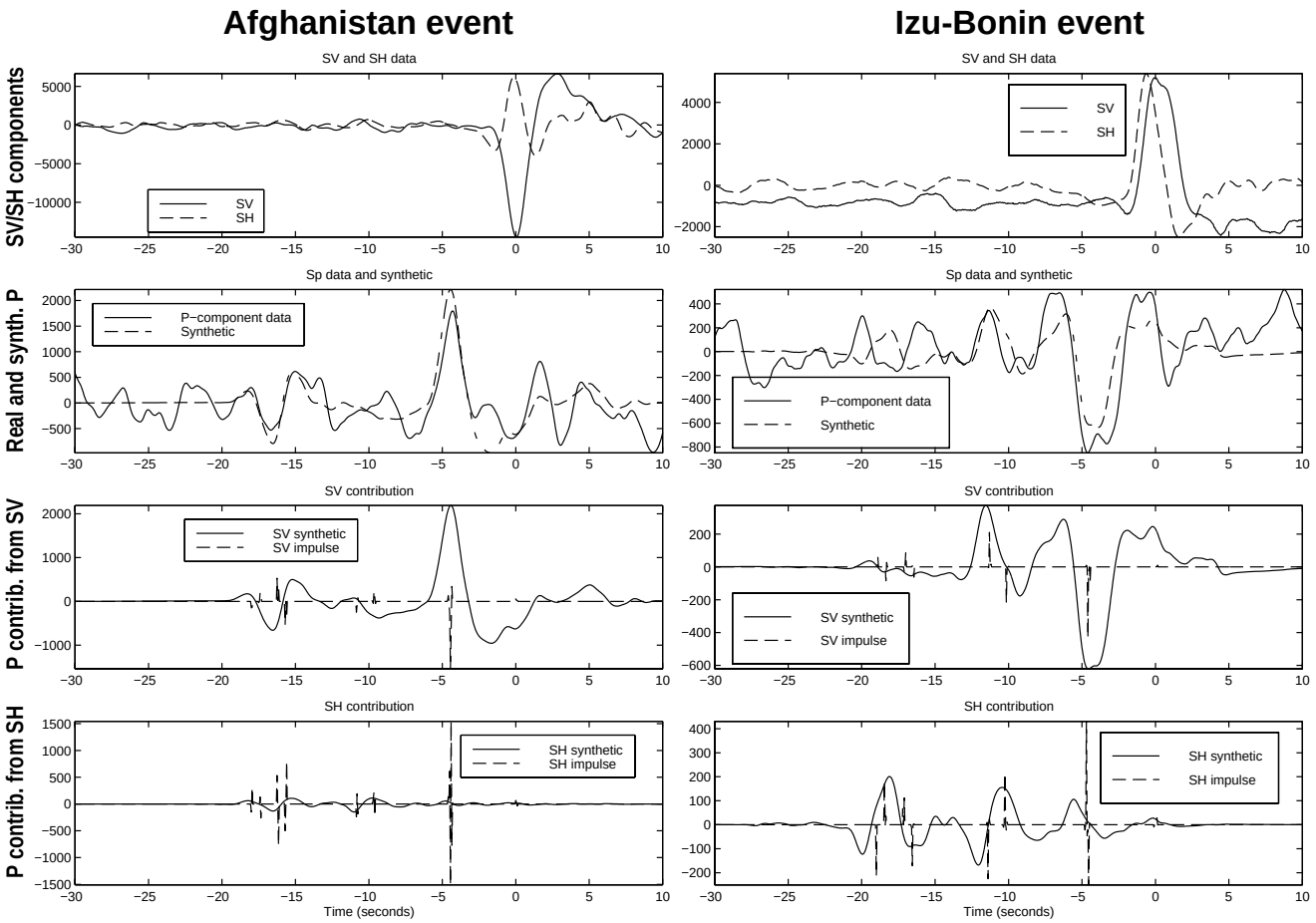

Figure 10. Two examples of *Sp* conversion data fits using events from Afghanistan and the Izu-Bonin Trench recorded at station YKW3 and described in Table 3. The uppermost panel shows the *SV* and *SH* arrivals; the next superimposes the real and synthetic *P* component. The lowermost two panels show the impulse responses and convolved *Sp* synthetics due to *SV*- and *SH*-polarization components, respectively.

5 CONCLUSIONS

The forward modelling technique presented here shows promise for extracting lithospheric structure from *P*- and *S*-wave data sets. As the example from station YKW3 illustrates, the technique should be particularly useful for analysis of data at individual, three-component, broad-band stations where underlying lateral heterogeneity may be accurately modelled in terms of anisotropic, dipping layers. Because the approach is ray-based and does not require shooting, it is sufficiently economical to be used as the basis for non-linear waveform inversion schemes. The development of such a scheme and its application to increasingly comprehensive data sets from stations of the global networks is the topic of ongoing research.

ACKNOWLEDGMENTS

Comments by Paul Richards and David Aldridge, reviews by Vadim Levin and John Diebold, and editorial commentary by Steven Ward led to substantial improvements in the manuscript. The Canadian National Seismograph Network and the Geological Survey of Canada provided data from station YKW3. This research was supported by NSERC grant #OGP 0138004.

REFERENCES

Aldridge, D.F., 1992. Analysis and inversion of seismic refraction traveltimes, *PhD thesis,* University of British Columbia, Vancouver.

Bock, G., 1994. Multiples as precursors to *S*, *SKS* and *ScS*, *Geophys. J. Int.,* **119,** 421–427.

Bostock, M.G., 1998. Mantle stratigraphy and evolution of the Slave province, *J. geophys. Res.,* **103,** 21 183–21 200.

Bostock, M.G., 1999. Seismic imaging of lithospheric discontinuities and continental evolution, *Lithos,* **48,** 1–16.

Booth, D.C. & Crampin, S., 1983. The anisotropic reflectivity technique; theory, *Geophys. J. R. astr. Soc.,* **72,** 755–766.

Cassidy, J.F., 1992. Numerical experiments in broadband receiver function analysis, *Bull. seism. Soc. Am.,* **82,** 1453–1474.

Červený, V., 1972. Seismic rays and ray intensities in inhomogeneous anisotropic media, *Geophys. J. R. astr. Soc.,* **29,** 1–13.

Diebold, J.B., 1987. Three-dimensional traveltime equation for dipping layers, *Geophysics,* **52,** 1492–1500.

Farra, V., Vinnik, L.P., Romanowicz, B., Kosarev, G.L. & Kind, R., 1991. Inversion of teleseismic *S* particle motion for azimuthal anisotropy in the upper mantle: a feasibility study, *Geophys. J. Int.,* **106,** 421–431.

Fryer, G.H. & Frazer, L.N., 1984. Seismic waves in stratified anisotropic media, *Geophys. J. R. astr. Soc.,* **78,** 691–710.

Gaherty, J.B. & Jordan, T.H., 1995. Lehmann discontinuity as the base of an anisotropic layer beneath continents, *Science,* **268,** 1468–1471.

Hake, H., 1986. Slant stacking and its significance for anisotropy, *Geophys. Prospect.,* **34,** 595–608.

Hales, A.L., 1969. A seismic discontinuity in the lithosphere, *Earth planet. Sci. Lett.,* **7,** 44–46.

Karato, S., 1992. On the Lehmann discontinuity, *Geophys. Res. Lett.,* **19,** 2255–2258.

Kennett, B.L.N., 1983. *Seismic Wave Propagation in Stratified Media,* Cambridge University Press, Cambridge.

Kennett, B.L.N., 1991. The removal of free surface interactions from three-component seismograms, *Geophys. J. Int.,* **104,** 153–163.

Langston, C.A., 1977. The effect of planar dipping structure on source and receiver responses for constant ray parameter, *Bull. seism. Soc. Am.,* **67,** 1029–1050.

Lehmann, I., 1961. *S* and the structure of the upper mantle, *Geophys. J. R. astr. Soc.,* **4,** 124–137.

Leven, J.H., Jackson, I. & Ringwood, A.E., 1981. Upper mantle seismic anisotropy and lithospheric decoupling, *Nature,* **289,** 234–239.

Levin, V. & Park, J., 1997. *P–SH* conversions in a flat-layered medium with anisotropy of arbitrary orientation, *Geophys. J. Int.,* **131,** 253–266.

Levin, V. & Park, J., 1998. *P–SH* conversions in layered media with hexagonally symmetric anisotropy: a cookbook, *Pure appl. Geophys.,* **151,** 669–697.

Revenaugh, J. & Jordan, T.H., 1991. Mantle layering from *S*cS reverberations 3: the upper mantle, *J. geophys. Res.,* **96,** 19 781–19 810.

Richards, P.G., Witte, D.C. & Ekström, G., 1991. Generalized ray theory for seismic waves in structures with planar nonparallel interfaces, *Bull. seism. Soc. Am.,* **81,** 1309–1331.

Rümpker, G. & Silver, P.G., 1998. Interpretation of shear-wave splitting observations in the presence of vertically-varying anisotropy, *Ann. Geophys.,* **16** (Suppl. 1), 157.

Savage, M.K., 1998. Lower crustal anisotropy or dipping boundaries? Effects on receiver functions and a case study in New Zealand, *J. geophys. Res.,* **103,** 15 069–15 087.

Silver, P.G. & Savage, M.K., 1994. The interpretation of shear-wave splitting parameters in the presence of two anisotropic layers, *Geophys. J. Int.,* **119,** 949–963.

Thomson, C.J., 1997. Modelling surface waves in anisotropic structures; I, Theory, *Phys. Earth planet. Inter.,* **103,** 3–4.

Vinnik, L.P., & Romanowicz, B. A., 1991. Origin of precursors to teleseismic *S* waves, *Bull. seism. Soc. Am.,* **81,** 1216–1230.

Woodhouse, J.H., 1974. Surface waves in a laterally varying layered structure, *Geophys. J. R. astr. Soc.,* **37,** 461–490.